

# Machine-Engineered Active Disorder for Digital Photonics

Jungmin Kim, Seungkyun Park, Sunkyu Yu,\* and Namkyoo Park\*

Resolving spatial and temporal complexities in wave–matter interactions is essential for controlling the light behavior inside disordered and nonstationary systems and therefore achieving high capacity devices. Although these complexities have usually been studied separately, a few examples exploiting both degrees of freedom have derived intriguing phenomena such as hyper-transport in evolving disorder and topological phenomena in synthetic dimensions. Here, engineering active disorder—disordered structures with external modulation—is proposed by employing deep neural networks. A functional regressor and a material evaluator are developed to enable inverse design of active disorder with target wave responses and evaluation of disordered structures according to the wave response controllability, respectively. By machine engineering deep-subwavelength disorder including a phase change material, functional disorder for light is revealed, which leads to angle-selective or broadband digital switching. A generative configuration of the neural network utilizing a single wave metric is also developed to realize a family of disordered structures with independent engineering of multiple wave properties, in contrast to the traditional engineering of disorder with a specific order metric. This approach establishes realization of reconfigurable devices by exploiting the spatiotemporal complexity in wave mechanics.

environments—is one of the important challenges for developing digital or analogue signal processing<sup>[1,2]</sup> and examining the complexity of dynamic systems.<sup>[3,4]</sup> The deterministic design of an active system is much more intricate than that of a passive system because the relationship between a system alteration and the following signal modulation is usually nonlinear,<sup>[5]</sup> even chaotic,<sup>[6]</sup> or abrupt.<sup>[7]</sup> In wave mechanics, the evolution of multifaceted wave degrees of freedom (frequency, canonical and angular momenta, and topology), even with a linear system modulation, is known to be generally nonlinear except for in the regime of small perturbations.<sup>[8]</sup> Furthermore, precise prediction or tailoring of active functionalities in wave-matter interactions becomes even more challenging with material or structural complexity, as shown in light flows in a disordered structure.<sup>[9,10]</sup> For example, the design of material perturbations for wave localization at a target position still remains a challenge, although landscape theory describes the extended boundary for the

spatial emergence of localization.<sup>[11,12]</sup> In this context, the development of a deterministic method that allows handling of correlated and vast numbers of degrees of freedom in active systems is strongly desired.


Recent advances in deep learning that have been applied to natural language processing,<sup>[13]</sup> computer vision,<sup>[14]</sup> and regression<sup>[15]</sup> have also been extended to physics problems, such as classical<sup>[16,17]</sup> and quantum mechanics,<sup>[18–20]</sup> fluid dynamics,<sup>[21]</sup> and photonics.<sup>[22–38]</sup> In these fields, the major focus is on the extraction of the relationship between signals and systems:<sup>[22–24]</sup> the inference of signal flows in a given system operating as instantaneous numerical solving of governing equations<sup>[21,25]</sup> or the construction of a system for a given signal flow operating as an inverse design process.<sup>[26–38]</sup> These data-driven approaches provide salient advantages over traditional numerical assessments in terms of extracting the nonlinear relationship between large system degrees of freedom by employing numerous synaptic parameters and neural activations in a deep neural network (DNN). However, the current approaches in this field still lack deep insights into active wave-matter interactions. For example, deterministic control of the system robustness or precise design of target functionalities in dynamic disordered systems have not been explored due to the inherent difficulty of resolving entangled material and dynamic complexities in wave–matter interactions.

## 1. Introduction

Understanding active systems—systems with signal flows dynamically tunable through interactions with their

J. Kim, S. Park, N. Park  
Photonic Systems Laboratory  
Department of Electrical and Computer Engineering  
Seoul National University  
Seoul 08826, Korea  
E-mail: nkpark@snu.ac.kr

J. Kim, S. Park, S. Yu  
Intelligent Wave Systems Laboratory  
Department of Electrical and Computer Engineering  
Seoul National University  
Seoul 08826, Korea  
E-mail: sunkyu.yu@snu.ac.kr

 The ORCID identification number(s) for the author(s) of this article can be found under <https://doi.org/10.1002/adom.202102642>.

© 2022 The Authors. Advanced Optical Materials published by Wiley-VCH GmbH. This is an open access article under the terms of the Creative Commons Attribution-NonCommercial-NoDerivs License, which permits use and distribution in any medium, provided the original work is properly cited, the use is non-commercial and no modifications or adaptations are made.

DOI: 10.1002/adom.202102642

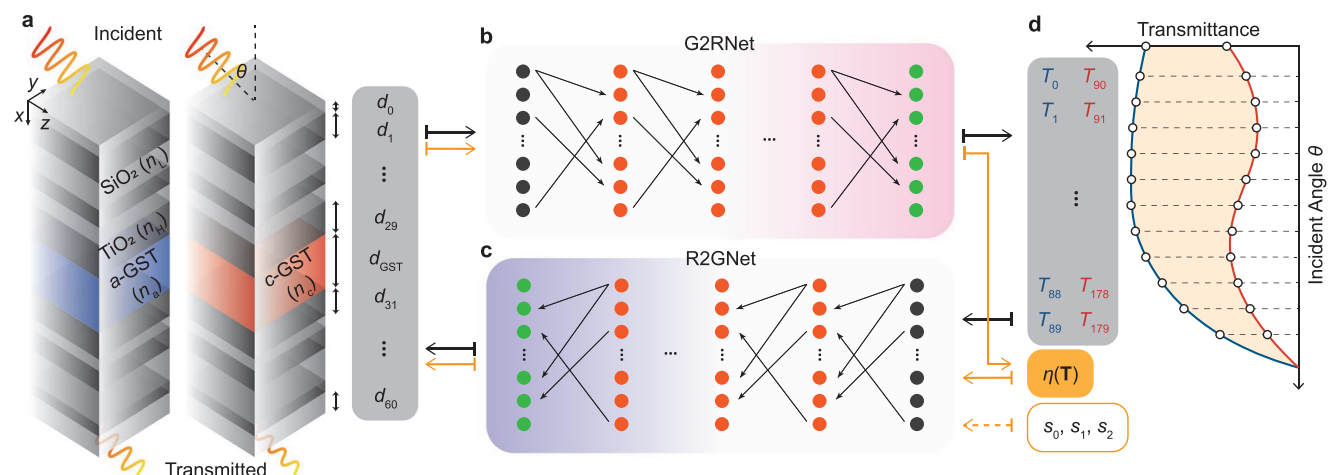


**Figure 1.** Active disorder and its DNN analysis. a) Sixty-one-layer (SiO<sub>2</sub>/TiO<sub>2</sub>) film including the core GST layer with interchangeable phases (*a*-GST, *c*-GST). b,c) Schematics of the fully connected (b) forward (G2RNet) and (c) backward (R2GNet) DNNs, mapping the (a) geometrical data  $\mathbf{d} = [d_0, d_1, \dots, d_{60}]$  and d) optical-response data  $\mathbf{T} = [\mathbf{T}^{(a)}, \mathbf{T}^{(c)}]$ .  $d_l$  is the thickness of the  $l^{\text{th}}$  layer ( $0 \leq l < 61$ ), with  $d_{30} = d_{\text{GST}} = 1 \mu\text{m}$ .  $d_l$  ( $l \neq 30$ ) has a value between 2 and 198 nm, while the GST layer thickness is fixed at  $d_{30} = d_{\text{GST}} = 1 \mu\text{m}$ . The structure is illuminated with a TE-polarized incident wave at angle  $\theta$ . The refractive indices of each medium are  $n_L = 1.43$  and  $n_H = 2.39$  for SiO<sub>2</sub> and TiO<sub>2</sub>, respectively,<sup>[66,67]</sup> and  $n_a = 3.96$  and  $n_c = 5.88$  for *a*-GST and *c*-GST, respectively.<sup>[68]</sup>  $T_m$  is measured in the range of  $0 \leq \theta < \pi/2$  for both GST phases (*a*-GST,  $0 \leq m < 90$ ; *c*-GST,  $90 \leq m < 180$ ). Black, orange, and green neurons represent input, hidden, and output layers, respectively.  $\eta(\mathbf{T})$  is the controllability of the optical transmittances. The prediction of and inverse design from the controllability with  $\eta$  are depicted by yellow arrows instead of black arrows.  $\mathbf{s} = [s_0, s_1, s_2]$  is the auxiliary random seed input discussed later.

In this paper, we show DNN-based engineering of active disorder for digital photonics. Employing the analogy between disordered materials and complex networks<sup>[9]</sup> and inspired by a study on target control of networks,<sup>[3]</sup> we investigate the disordered structure with a target activation region for modulation. The relationship between disorder landscapes and actively controlled and tunable angular transmittances is then analyzed with a functional regressor and a material evaluator, which are composed of tandem DNN structures.<sup>[20,26–28]</sup> This DNN analysis enables deterministic design of digital functional devices: angle-selective or broadband switching of light. By machine learning the relationship between an order metric and the controllability of angular responses, we suggest a wave-response-based classification of active disorder, which subdivides the vague regimes in traditional, material-based classifications.<sup>[39,40]</sup> Our results provide a solution for handling the complex interactions among spatial disorder, dynamic modulations, and wave responses, leading to extended design freedom for digital photonics.

## 2. Model Definition

As an example of active light-matter interactions in a potential landscape of an arbitrary layout, we focus on the angular scattering response of a 1D disordered platform with an active layer. With large degrees of freedom for disorder, the statistical relationship between disordered patterns and wave localization includes both bulk and interface interference effects<sup>[41]</sup> violating effective medium theory (EMT), which hinder the deterministic design of a 1D film even for the passive angular response. The problem becomes even more complex when active modulation alters the interference inside the system. Considering critical applications of this platform, including transparent displays,<sup>[42]</sup>

organic light-emitting diodes (OLEDs),<sup>[43]</sup> and spatial light modulators (SLMs),<sup>[44]</sup> we employ DNNs<sup>[45]</sup> for dual-spectral optimization to address this problem.

As an example platform, we consider a SiO<sub>2</sub>-TiO<sub>2</sub> multi-layer disordered structure with the core layer substituted by the phase change material Ge<sub>2</sub>Sb<sub>2</sub>Te<sub>5</sub> (GST). The detailed structure is shown in Figure 1a with its layer thicknesses  $\mathbf{d} = [d_0, d_1, \dots, d_{60}]$ . Under transverse electric (TE)-polarized incidence of wavelength  $\lambda_0 = 2500 \text{ nm}$ , we examine the active control of the optical angular transmittance through the disordered structure by employing the phase change of the GST material (*a*-GST and *c*-GST for amorphous and crystalline phases, respectively<sup>[46]</sup>) in the core layer. The wave response of active disorder is quantified in the form of dual angular spectra for each GST phase:  $\mathbf{T} = [\mathbf{T}^{(a)}, \mathbf{T}^{(c)}]$ , where the components of each vector  $T_m^{(a,c)}$  are the transmittances at a discretized incident angle between 0° and 90° (Figure 1d). The main problem then becomes the extraction of the relationship between a set of structural parameters  $\mathbf{d}$  and the dual-spectral angular responses  $\mathbf{T}$  while the GST layer provides a fixed modulation to the disordered platform. The data for the DNNs are obtained through the transfer matrix method (TMM) as a ground truth (see the Experimental Section).

## 3. DNN as a Functional Regressor

One of the major hurdles in the DNN inference of the relationship between light and matter is the one-to-many correspondence between a wave response and photonic structures. This issue is critical not only in guaranteeing stability during the DNN training but also in covering a wider design space in the inverse design of photonic structures from the target optical response. In resolving the one-to-many correspondence in deep-learning photonics, two related methodologies have been

**Table 1.** MSEs of the G2RNet and R2GNet for test datasets.

Data set	# Samples	$d_i$ range [nm]	G2RNet [ $10^{-4}$ ]	R2GNet [ $10^{-4}$ ]
I	833	(2, 98)	1.54	15.15
II	833	(2, 118)	2.38	39.30
III	834	(2, 138)	2.63	12.33
IV	834	(2, 158)	4.57	10.44
V	833	(2, 178)	7.25	11.06
VI	833	(2, 198)	15.77	13.07
Overall	5000	(2, 198)	5.69	16.89

proposed according to the covered range of the design space.<sup>[23]</sup> First, by using pretrained DNNs for the inference of wave behaviors, the construction of the tandem inverse-design networks<sup>[20,26–28]</sup> or the secondary learning of input photonic structures<sup>[37]</sup> have been proposed. With stable and efficient learning of DNNs, those methods allow for the coverage of a part of the complete design space. On the other hand, more complex network architectures with intensive training processes have also been studied to extract multiple branches of the photonic structures for the target optical response, as demonstrated with mixture-density DNNs,<sup>[35,36]</sup> multibranch DNNs,<sup>[38]</sup> and deep generative models.<sup>[29–31]</sup> In this section, to efficiently find a photonic structure for the target active functionality, we employ the tandem network with pretrained forward DNNs.<sup>[26]</sup>

For this goal, we construct fully connected DNNs mapping the structural parameter space to the angular response space (Geometry-to-Response, G2RNet) and vice versa (Response-to-Geometry, R2GNet; see Experimental Section and Note S1 in the Supporting Information for details of the DNNs). We first train G2RNet for the prediction of optical responses by employing randomly generated structures and their TMM-calculated responses as input and output datasets, respectively. The cost function for the ON–OFF dual-spectral optimization is defined by the mean squared error (MSE) loss over  $T$

$$L = \frac{1}{180} \sum_{m=0}^{179} |\hat{T}_m - T_m|^2 \quad (1)$$

where  $\hat{T}_m$  and  $T_m$  are the G2RNet-predicted and ground-truth transmittances, respectively. The G2RNet-based prediction allows for higher computation speed and therefore handling of huge datasets (total of  $2 \times 10^6$  realizations).

We employ the pretrained G2RNet to obtain expected optical responses from the geometry output of R2GNet. The MSE cost function that compares these responses with TMM-calculated optical responses then allows stable optimization of R2GNet, resolving the one-to-many correspondence issue between an optical response and the geometry.<sup>[20,26]</sup> After the training, we can extract the inversely designed realization  $d_i$  at the intermediate layer of cascaded R2GNet-G2RNet for a given target response.

After training the G2RNet and R2GNet, we verify the results with the test dataset. Same as the training dataset (Note S1, Supporting Information), the test set is also partitioned into the subclasses I–IV according to the maximum allowed value of  $d_i$

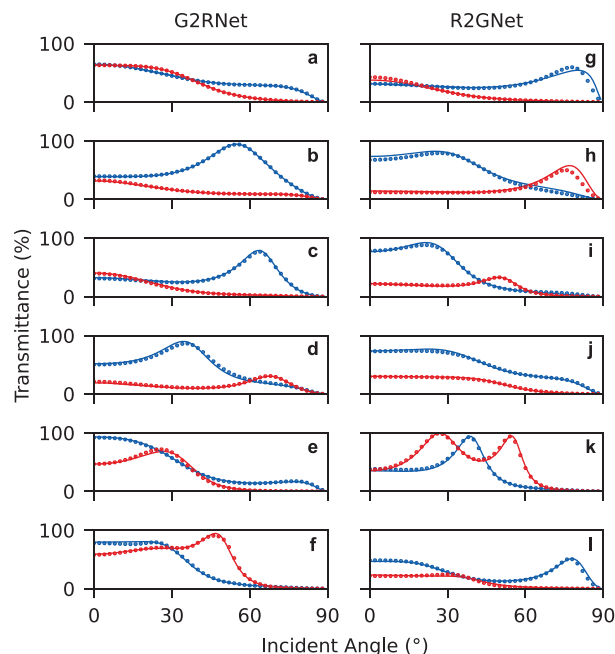


**Figure 2.** Inference by trained DNNs: a–f) G2RNet and g–l) R2GNet. Each realization of the a,g) subclass I, b,h) subclass II, c,i) subclass III, d,j) subclass IV, e,k) subclass V, and f,l) subclass VI. The solid lines and symbols denote the ground truth and DNN results, respectively. Red and blue color denote the responses for  $a$ -GST and  $c$ -GST phases.

(Table 1). As shown in Table 1, both DNNs provide the excellent agreements with the ground truth, achieving the MSE  $\approx 5.69 \times 10^{-4}$  for the G2RNet and  $1.69 \times 10^{-3}$  for the R2GNet (see Figure 2a–f for each subclass realization of the G2RNet and Figure 2g–l for each subclass realization of the R2GNet).

We demonstrate two examples of target active functionalities defined for the angular response. Both examples correspond to data-driven extraction of the nonlinear relationship between the sets of  $\approx 10^2$  variables ( $d$  and  $T$ ), which include the interferences of multiple scatterings altered by the GST phase transition. The first example is active control of highly selective angular filtering, which is a critical functionality for SLMs, holography, and privacy films. We model the selectivity of target responses with the Lorentzian line shape:

$$T^{(a,c)}(\theta) = \left[ 1 + 4 \left( \frac{\theta - \theta_{a,c}}{\theta_{FWHM}} \right)^2 \right]^{-1} \quad (2)$$

where  $T^{(a)}$  and  $T^{(c)}$  correspond to the angular transmittances for the  $a$ -GST and  $c$ -GST phases with angular peaks  $\theta_a = 30^\circ$  and  $\theta_c = 60^\circ$ , respectively, and  $\theta_{FWHM} = 12^\circ$  defines the angular selectivity with the full width at half maximum (FWHM, Figure 3a).

The trained DNNs successfully lead to the target angle-selective filter and its digital switching operation with the designed structural parameters (Figure 3b). The TMM-calculated “true” responses (symbols in Figure 3a) and the 2D TMM simulation (Figure 3c,d) verify that the designed realization operates well for active tuning between  $a$ - and  $c$ -GST phases; for point-source-like incidence, only a narrow range

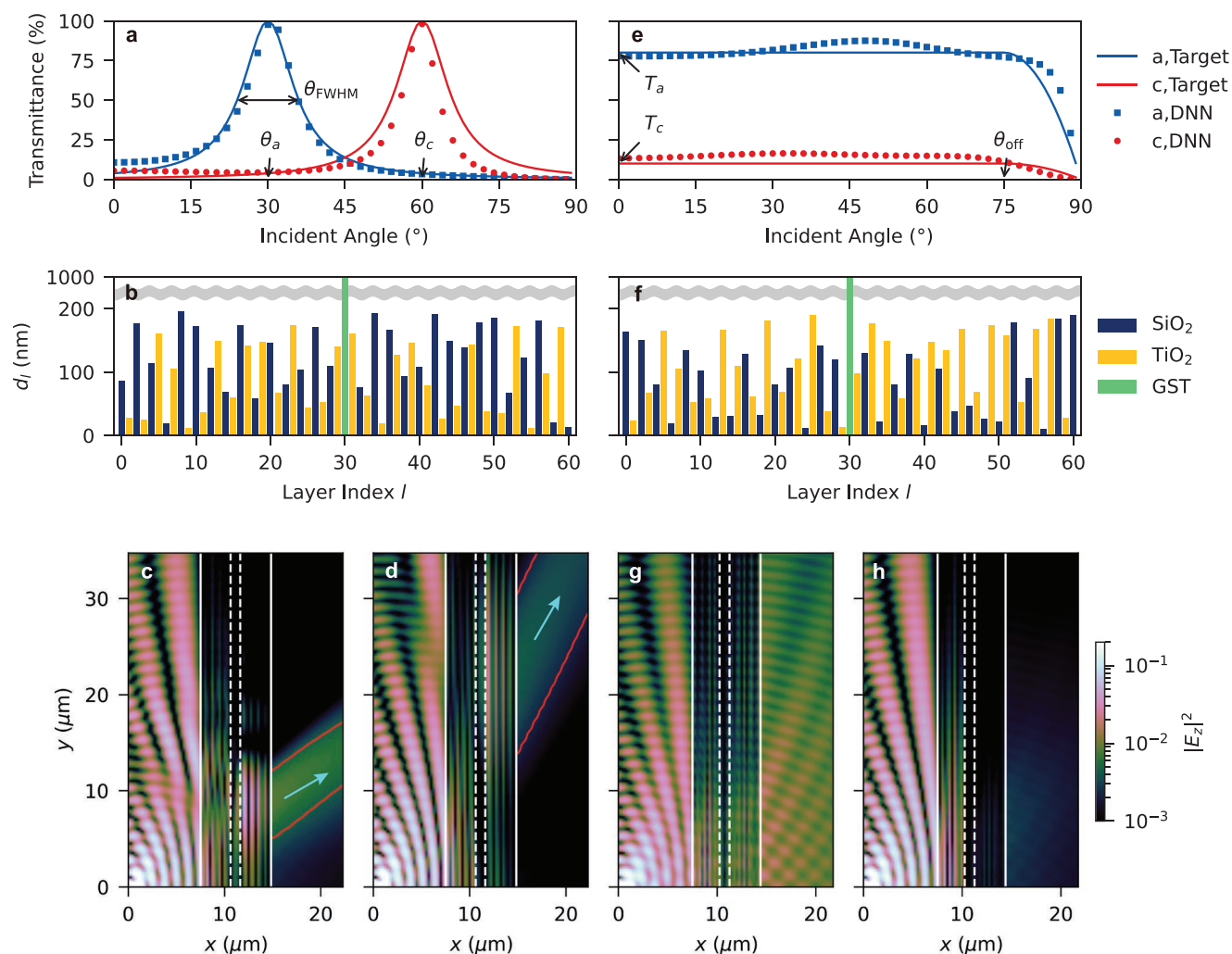


**Figure 3.** DNN functional regressor. a–d) Angle-selective and e–h) broadband active switching devices. a,e) Target responses (solid lines) and DNN results (symbols, marked every 2°) for active responses of both functionalities: blue and red for *a*-GST and *c*-GST responses, respectively.  $\theta_{a,c}$ : target angles for selective transparency,  $\theta_{FWHM}$ : target broadening,  $T_{a,c}$ : target transmission levels, and  $\theta_{off}$ : cutoff angle. b,f) Corresponding disordered structures (navy, yellow, and green bars for  $\text{SiO}_2$ ,  $\text{TiO}_2$ , and GST layers, respectively) inversely designed from the target responses by R2GNet. c,d,g,h) 2D intensity profiles  $|E_z|^2$  for both phases of designed devices: c,g) *a*-GST and d,h) *c*-GST. The red lines in (c,d) indicate the contour for the half maximum of the intensity in the transmission part.

of angular components is transmitted near the target angle (30° and 60° for *a*- and *c*-GST). Notably, R2GNet provides systematic inverse design of active switching, in sharp contrast to previous approaches:<sup>[47–50]</sup> analytical methods<sup>[47,48]</sup> that are restricted to the approximation of simplified platforms or heuristic approaches with numerical methods<sup>[49,50]</sup> that are separately developed for each specific platform. We emphasize that this deterministic handling of active responses is enabled by the ON-OFF dual-spectral optimization of G2RNet and R2GNet.

The second example is a counterpart of the first one in terms of spectral richness: full broadband switching with an extreme modulation depth, which enables switching between completely transparent and opaque films independent of incident angle. The target transmission response is modelled by the flat function with high  $\theta$  suppression

$$T^{(a,c)}(\theta) = \begin{cases} T_{a,c}, & \theta < \theta_{off} \\ \frac{T_{a,c}(90^\circ - \theta)(\theta - 2\theta_{off} + 90^\circ)}{(90^\circ - \theta_{off})^2}, & \theta \geq \theta_{off} \end{cases} \quad (3)$$

where  $T_a = 0.85$  and  $T_c = 0.1$  are the target transmittance levels for the *a*-GST and *c*-GST phases, respectively, and  $\theta_{off} = 75^\circ$  denotes the assigned cutoff angle for physical validity near the angular limit  $\theta \rightarrow 90^\circ$ . Using R2GNet, we achieve the target response (Figure 3e) with the designed parameters (Figure 3f), leading to nearly complete transparency and opaqueness for the point-source-like incidence (Figure 3g,h; Note S2 in the Supporting Information for details). While this functionality is a critical feature for transparent displays and tunable backlight in liquid crystal displays, it is unachievable in crystals with inherent anisotropy and in uncorrelated disordered systems



with suppressed transport but is enabled by machine engineering of disordered platforms. We conduct extended analysis for the comparison of the TMM results with the results from the finite element method (Note S3, Supporting Information) and for the regressor model performance for different performance metrics and target parameters (Note S4, Supporting Information).

#### 4. DNN as a Material Evaluator

Having achieved inverse design of the platform for dynamic designer responses, we further extend our study to reveal the mechanism underlying light-matter interactions in machine-engineered active disorder, for example, the introduction of a family of disorder classified by its controllability. Despite recent efforts to classify disordered materials,<sup>[40]</sup> such classifications according to various order metrics usually do not fully guarantee the expected wave properties and a successful inverse design procedure due to the nonlinear relationship between structural information and multiple interrelated wave properties.<sup>[9]</sup> Notably, in terms of active devices, such properties need to include the responsivity to active modulation, for example, the dynamic change in wave properties induced by the modulation of disordered materials. For this purpose, we introduce a single parameter that enables the measuring of wave properties related to active modulation, the “controllability metric”

$$\eta \equiv \left( \frac{1}{90} \sum_{m=0}^{89} |T_m^{(a)} - T_m^{(c)}|^2 \right)^{1/2} \quad (4)$$

which is the wave counterpart of an order metric for disordered materials. This controllability metric  $\eta$  quantifies the efficiency in controlling the transmittance through a sample according to the material transition between the GST states:  $\eta = 0$  for perfectly modulation-immune platforms and  $\eta = 1$  for the complete transition between omnidirectional transparent and opaque states. As a bridge to traditional studies on disordered materials,<sup>[40]</sup> we then try to examine the relationship between a proper order metric and the controllability metric  $\eta$  as a criterion for the evaluation of the degree of disorder in terms of its active wave properties.

Because the method employed in Section 3 allows only the coverage of a part of the entire design space, it is necessary to expand the covered design space in order to statistically examine the material properties of a family of disordered structures for a given  $\eta$ . For this purpose, we modify the DNN in Figure 1 to have 1 informative and 3 auxiliary inputs instead of using the multidimensional space for the discretized angular responses  $T$ . First, a single controllability metric  $\eta$  is employed as the output for the modified G2RNet (mG2RNet) and the input for the modified R2GNet (mR2GNet), as shown in Figure 1b,c (yellow arrows). Most importantly, we newly introduce the 3D seed  $\mathbf{s} = [s_0, s_1, s_2]$  as an auxiliary input for the mR2GNet, where each  $s_{0-2}$  has a random value between 0 and 1 with a uniform random distribution. We conduct mR2GNet training using expected optical responses obtained from mG2RNet, following the same process as in Figure 1. When successfully training the

mR2GNet with ground-truth responses ( $\eta$  for  $\mathbf{d}$ ) and random seeds ( $\mathbf{s}$ ), the network constructs the one-to-one correspondence between  $(\eta, \mathbf{s})$  and  $\mathbf{d}$ , which naturally leads to the one-to-many correspondence between  $\eta$  and  $\mathbf{d}$  due to diverse values of  $\mathbf{s}$  (Figure 4a). Therefore, as similar to multibranch DNNs<sup>[38]</sup> or deep generative models,<sup>[29–31]</sup> the suggested mR2GNet allows the extraction of multiple branches of the photonic structures for the target controllability  $\eta$ , which realizes a family of active disorder for a given  $\eta$ . Notably, when compared with multibranch DNNs,<sup>[38]</sup> our approach is especially proper to the problems in disordered photonics, because the continuous profile of  $\mathbf{s}$  is proper to handle disordered materials, which are quantified by continuous perturbation values, not by quantized values. In Note S5 in the Supporting Information, we study the evolution of the structural statistics and  $\eta$  accuracy with the trained mR2GNet, which demonstrates the physical validity of mR2GNet in terms of continuous phase transition in the range of  $0.05 \leq \eta \leq 0.6$ .

Figure 4b–j shows an example of generating a family of active disorder: the ensembles of three different controllability metrics  $\eta = 0.05, 0.3$ , and  $0.6$ , which are obtained with multiple combinations of random seeds (see Note S5 and Movies S1 and S2 (Supporting Information) for the validity of the material evaluator). Although we can assume hypothetically infinite pairs ( $a$ - and  $c$ -GST) of angular transmittances for a given  $\eta$ , mR2GNet filters the subsets of physically allowed optical responses with the structural variety of a family of active disorder (Figure 4b–d). Notably, each material phase defined by  $\eta$  supports distinctive statistics for both structural (Figure 4e–g) and optical (Figure 4h–j) realizations. We further study the field profiles and perform a comparison with EMT (Note S6, Supporting Information), showing that mR2GNet enables efficient inverse design in the deep-subwavelength regime that violates EMT.

We examine the structural and wave properties of active disorder in different regimes, clarifying the uniqueness of each regime. In line with the broad angular responses (Figure 4h,j), robust ( $\eta = 0.05$ , Figure 4b) or sensitive ( $\eta = 0.6$ , Figure 4d) active disorder possesses more randomized structures than intermediate disorder ( $\eta = 0.3$ , Figure 4c). Although highly randomized structures (Figure 4b,d) and their statistics (Figure 4e,g) appear similar at a glance, the DNN-based design of distinctive patterns results in completely contrasting wave dynamics: the “hiding” of the GST core layer (Figure 4h) or almost “omnidirectional” switching (Figure 4j) by disordered multilayer claddings. As shown by each error bar height in Figure 4b–d, the realization number of physically acceptable high-controllability responses ( $\eta = 0.6$ , Figure 4d) is limited compared to that of low-controllability cases (Figure 4b,c) because the possible spectra for high  $\eta$  are inevitably limited.

In the intermediate regime (Figure 4c), the structures are close to the deformation of a crystalline profile rather than to uncorrelated disorder, possessing Gaussian-like structural statistics with narrow deviations (Figure 4f). This set of structures leads to various candidates for an angle-selective switching operation (Figure 4i), which is in line with previous studies on the relationship between crystals and their narrow angular responses.<sup>[51]</sup> Overall, the demonstrated grouping of various candidates of disorder by  $\eta$  provides a novel material evaluation based on wave responses.

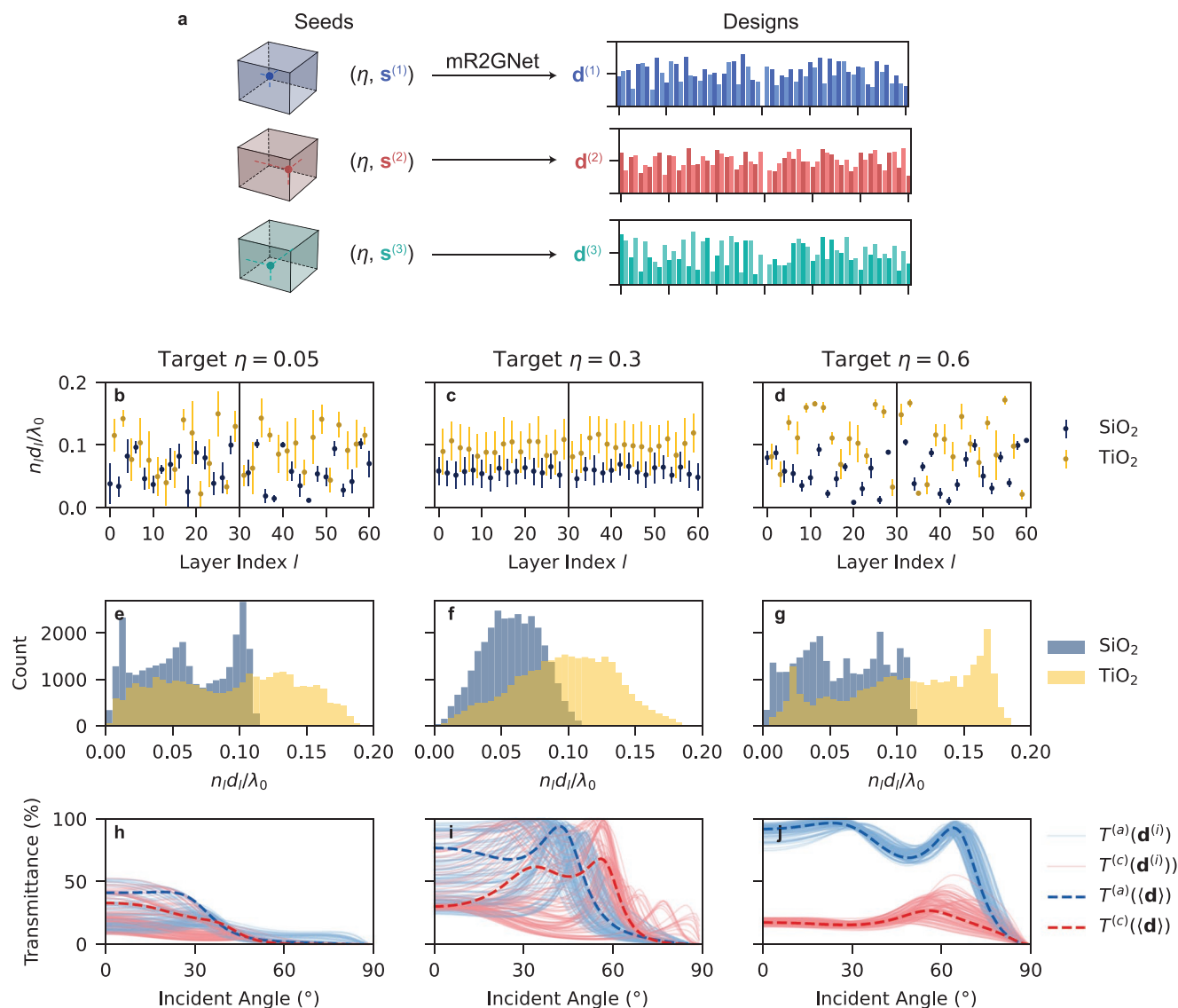


**Figure 4.** DNN material evaluator. a) A schematic of the function of the mR2GNet expanding the design space. The multiple outputs  $\mathbf{d}^{(n)}$  having the identical target controllability  $\eta$  are obtained through the mR2GNet with different random seeds  $\mathbf{s}^{(n)}$ , which is selected from the space (colored boxes) with the uniform random distribution. b–j) Inverse design examples with target controllability metrics. b–d) Ensemble distributions of optical phase evolution  $n_l d_l$  in each layer of the designed structures. e–g) Statistical distributions of optical phase evolution  $n_l d_l$ . h–j) Corresponding angular responses for different GST phases (solid lines, blue for *a*-GST and red for *c*-GST), and ensemble-averaged results from the averaged structural parameters  $\langle \mathbf{d} \rangle$  (dashed lines). b,e,h)  $\eta = 0.05$ ; c,f,i)  $\eta = 0.3$ ; d,g,j)  $\eta = 0.6$ . We plot an ensemble of 1000 realizations for (b–g) and an ensemble of 100 realizations for (h–j) for visibility. All other parameters are the same as those in Figure 3.

## 5. Engineered Active Disorder

Compared with the traditional view on disordered photonics—classifying disordered structures based on order metrics and then examining the wave behaviors in each class of disorder—our data-driven approach in Figure 4 provides a distinctive viewpoint on light-disorder interactions, which originates from the classification of “wave behavior.” To characterize the wave behavior, we utilize two parameters: the angle-averaged transmittance  $T_{\text{avg}} \equiv \sum_{m=0}^{89} (T_m^{(a)} + T_m^{(c)}) / 180$  and the controllability metric  $\eta$ , which evaluate the average and modulation depth of the transparency of a sample, respectively. The structural

property of a material is quantified by the translational order metric  $\tau$  defined in Refs.<sup>[39,40]</sup> which tends to increase from  $\tau = 0$  to  $\tau = \tau_c$  when the material microstructure changes from uncorrelated disorder to crystalline order (see the Experimental Section for the definition of  $\tau$  and the setting of  $\tau_c$ ).

Figure 5a shows the 3D plot of the relationship among  $T_{\text{avg}}$ ,  $\tau$ , and  $\eta$  obtained from the inverse design with a given  $\eta$ . The extension of the design space in the mR2GNet is demonstrated allows for the handling of the order metric  $\tau$  from 0 to  $\approx 0.5\tau_c$ , achieving the one-to-many correspondence between a wave property ( $\eta$ ) and material profiles ( $\tau$ ). The result also clarifies the evolution of the average transparency and its tunability with respect to the degree of disorder. As predicted in Figure 4 and

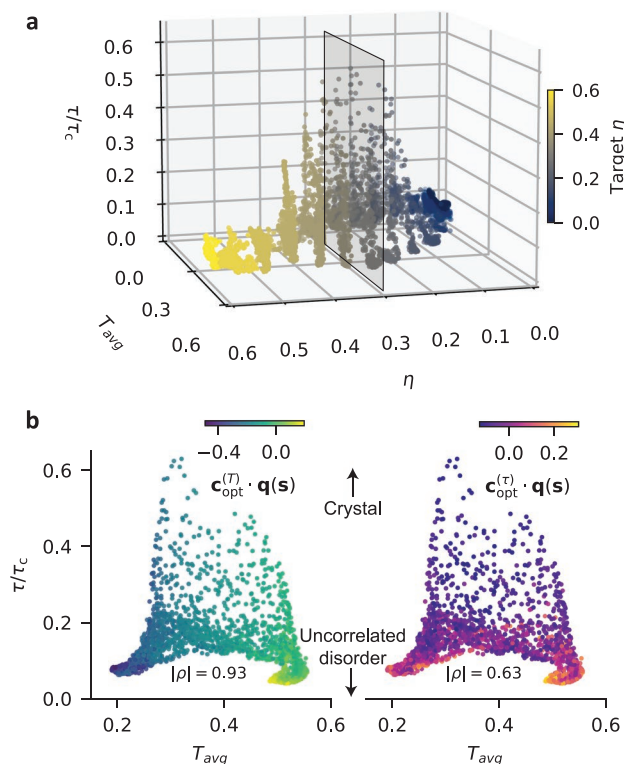


**Figure 5.** Engineered active disorder. a) Distribution of the designed realizations in the 3D parameter space defined by the angle-averaged transmittance  $T_{\text{avg}}$ , translational order metric  $\tau$ , and obtained controllability metric  $\eta$ . The target controllability  $\eta$  is represented by gradual colours. b) 2D ( $T_{\text{avg}}$ ,  $\tau$ ) projections of the data points with the target  $\eta = 0.3$  (the transparent window in (a)). Left and right panels are coloured for differently optimized functions of random seeds:  $\mathbf{c}_{\text{opt}}^{(\tau)} \cdot \mathbf{q}(\mathbf{s})$  and  $\mathbf{c}_{\text{opt}}^{(T)} \cdot \mathbf{q}(\mathbf{s})$  with respect to  $T_{\text{avg}}$  and  $\tau$ , respectively. All other parameters are the same as those in Figure 3.

per the traditional understanding of the relationship between angular responses and disorder strength,<sup>[52]</sup> highly tunable ( $\eta \approx 0.6$ ) or highly robust ( $\eta \approx 0.0$ ) structures that possess broadband responses (Figure 4c,i) are obtained with strong disorder ( $\tau \approx 0$ ).

Furthermore, more intriguing phenomena are observed in the intermediate regime:  $\eta \approx 0.3$ , which includes the angle-selective digital switching platforms in Figure 3a. In this regime, there are large degrees of freedom in the transparency  $T_{\text{avg}}$  because there could exist multiple pairs of ON–OFF angular profiles with the same tunability. Even at almost the same  $T_{\text{avg}}$ , a number of disorder realizations are therefore obtained with different values of  $\tau$ . The DNN-based design in this case then discovers a new grouping of disordered structures not by structural metrics but by similar optical responses. This result also confirms that the traditional method for designing disorder—the inverse design of materials from  $\tau$ —cannot pave a direct route to wave responses such as  $\eta$  or  $T_{\text{avg}}$ . In this context, our application of DNNs provides a clue to resolving the multidimensional complexity in the field of “engineered disorder.”<sup>[9]</sup>

Successfully classifying disordered structures by their controllability  $\eta$ , a natural question then arises in terms of the inverse design process: “can we control other wave or matter quantities while preserving the target optical response (here,

$\eta$ )?” which is a core concept of engineered disorder.<sup>[9]</sup> The key parameter for this question is assessed with the 3D random seed input  $\mathbf{s} = [s_0, s_1, s_2]$  to the mR2GNet. Each  $\mathbf{s}$  generates a specific realization of an ensemble of disordered structures, which constitute a group of materials classified by  $\eta$ . For this group of materials, we examine the effect of the seed  $\mathbf{s}$  on the other optical response ( $T_{\text{avg}}$ ) and order metric ( $\tau$ ) to bridge the machine learning classification and traditional theory of disordered photonics.

Considering  $0 \leq s_r \leq 1$  for  $r = 0, 1, 2$ , we examine the influence of  $\mathbf{s}$  up to its second-order contributions by defining  $\mathbf{q}(\mathbf{s}) = [s_0, s_1, s_2, s_0s_1, s_1s_2, s_2s_0, s_0^2, s_1^2, s_2^2]$ . If we can derive the relationship  $X \approx \mathbf{c}^{(X)} \cdot \mathbf{q}(\mathbf{s})$  for a given  $\eta$ , where  $X = T_{\text{avg}}$  or  $\tau$ , then deterministic handling of optical ( $T_{\text{avg}}$ ) or structural ( $\tau$ ) responses will be allowed by obtaining a group of  $\mathbf{s}$  from  $X \approx \mathbf{c}^{(X)} \cdot \mathbf{q}(\mathbf{s})$ . Focusing on the case of  $\eta = 0.3$ , we therefore optimize  $\mathbf{c}^{(X)} = \mathbf{c}_{\text{opt}}^{(X)}$  with an ensemble of the results from mR2GNet (Figure 5a) to maximize the correlation between  $f(\mathbf{s}; \mathbf{c}) = \mathbf{c}^{(X)} \cdot \mathbf{q}(\mathbf{s})$  and  $X$  (see Experimental Section and Note S7 (Supporting Information) for details of the optimization). Notably,  $\mathbf{c}_{\text{opt}}^{(X)}$  describes the contribution of each element of  $\mathbf{q}(\mathbf{s})$  to the mR2GNet inference of  $T_{\text{avg}}$  or  $\tau$ .

Figure 5b,c show the maps of the optimized representation  $f(\mathbf{s}; \mathbf{c} = \mathbf{c}_{\text{opt}}^{(X)}) = \mathbf{c}_{\text{opt}}^{(X)} \cdot \mathbf{q}(\mathbf{s})$  for  $X = T_{\text{avg}}$  and  $X = \tau$ , providing strong positive (Figure 5b) or negative (Figure 5c) correlations of  $T_{\text{avg}}$  or  $\tau$  with  $f(\mathbf{s}; \mathbf{c} = \mathbf{c}_{\text{opt}}^{(X)})$ , respectively. The optimized correlations  $\rho_{f,T}$  and  $\rho_{f,\tau}$  between the function  $f$  and the engineered responses have absolute values up to 0.93 and 0.63, respectively, leading to excellent matching to wave ( $T_{\text{avg}}$ ) and matter ( $\tau$ ) quantities. We note that even a linear representation with  $\mathbf{q}(\mathbf{s}) = [s_0, s_1, s_2]$  provides a reasonable approximation of these quantities (see Note S7 in the Supporting Information), demonstrating the distinct contribution of  $\mathbf{s}$  elements to each wave/matter response from the mR2GNet design.

## 6. Conclusion

To summarize, we employed the strength of machine learning approaches in the engineering of active disorder. Two different configurations of DNNs are applied to realize a specific disordered platform and a family of disordered structures. First, we demonstrated inverse design of disorder with a target functionality for an angular transmittance example. The results include practical applications such as angle-selective and broadband switching devices. Second, the evaluation and engineering of the degree of disorder in terms of controllability was demonstrated using the DNNs with random seeds. This approach based on a single target parameter (here, the controllability metric) discovers a family of disordered structures that allows independent control of multiple wave properties.

We note that the evaluation of active disorder according to the controllability provides a novel viewpoint on understanding the microstructures of materials in terms of wave responses. The classes of materials defined by different values of  $\eta$ , which had been included in the same class for the traditional order metric  $\tau$ , provide significantly distinct active responses. As shown in the large- $\eta$  design, the responses include global control of the entire system with a local manipulation (here,

the GST layer) analogous to the hub modulation in scale-free networks.<sup>[53]</sup> From this viewpoint, the small- $\eta$  design robust to GST modulation corresponds to disconnection of the links to the GST layer through destructive interference.

Our machine learning inverse design provides clear advantages in terms of handling spatial and temporal complexities compared with previous design strategies. For example, although numerous studies have been performed on 1D disorder in the context of diagonal<sup>[54]</sup> and off-diagonal<sup>[55]</sup> disorder, crystalline<sup>[56]</sup> or disordered<sup>[41]</sup> subwavelength structures, and correlated disorder,<sup>[57,58]</sup> all of these works have employed stationary structures, lacking active control of optical responses. Previous studies on active photonic devices have also been restricted to the modulation of ordered structures of small perturbations.<sup>[59–62]</sup>

In addition to intriguing works in deep-learning photonics, including the design of nanostructures,<sup>[24,25,31]</sup> metamaterials<sup>[27,29,30]</sup> and metasurfaces,<sup>[33]</sup> holography,<sup>[32]</sup> our study on active photonic functionalities in disordered platforms will provide additional degrees of freedom in the application of deep-learning to light-matter interactions, paving the way to the handling of spatially-complex and dynamical systems. Although we examined one of the optical responses as an example—angular transmittance—the versatile features of the DNNs will enable engineering of not only the other responses (spectral responses, angular momenta, topology) but also their mixtures: the design of active disorder in the intermediate regime,<sup>[9]</sup> temporal disorder,<sup>[63]</sup> and disordered topological phenomena.<sup>[7]</sup> As shown in the analogy between GST-controlled disorder and target control of complex networks,<sup>[3]</sup> our machine learning strategy can also be extended to other fields beyond wave mechanics, such as the interpretation and design of evolving complex networks.

## 7. Experimental Section

**TMM:** To calculate optical responses, we apply the TMM to 1D multilayers. Given the refractive index  $n_l$ , relative wave impedance  $Z_l$ , and thickness  $d_l$  of the  $l$ -th layer in addition to the external refractive index  $n_{\text{ext}}$ , impedance  $Z_{\text{ext}}$ , and incident angle  $\theta$ , the transfer matrix of the system of total  $L$  layers for TE polarization becomes

$$M = A_{\text{ext}}^{-1} \cdot \prod_{l=1}^L (A_{L-l} B_{L-l} A_{L-l}^{-1}) \cdot A_{\text{ext}} \quad (5)$$

where

$$\begin{aligned} A_l &= \begin{bmatrix} 1 & 1 \\ k_l^\perp / n_l Z_l k_0 & -k_l^\perp / n_l Z_l k_0 \end{bmatrix}, \\ A_{\text{ext}} &= \begin{bmatrix} 1 & 1 \\ \cos\theta / Z_{\text{ext}} & -\cos\theta / Z_{\text{ext}} \end{bmatrix}, \\ B_l &= \begin{bmatrix} \exp(ik_l^\perp d_l) & 0 \\ 0 & \exp(-ik_l^\perp d_l) \end{bmatrix} \end{aligned} \quad (6)$$

are the matrices representing the boundary conditions ( $A_l$  and  $A_{\text{ext}}$ ) and intralayer propagation ( $B_l$ ) on the forward ( $[1, 0]^T$ ) and backward ( $[0, 1]^T$ ) wave basis vector,  $k_l^\perp = k_0 \sqrt{n_l^2 - n_{\text{ext}}^2 \sin^2 \theta}$  is the longitudinal

component of the wavevector in each layer, and  $k_0 = 2\pi/\lambda_0$  is the free-space wavenumber. The reflectance ( $R = |r|^2$ ) and transmittance ( $T = |t|^2$ ) of the structure as functions of the incident angle are then obtained through the following relation

$$M \begin{bmatrix} 1 \\ r \end{bmatrix} = \begin{bmatrix} t \\ 0 \end{bmatrix} \quad (7)$$

**DNN Parameters:** G2RNet is composed of an input layer (61 neurons), 10 hidden layers (180 neurons for each layer, which are all batch-normalized<sup>[64]</sup> and activated by the GELU function<sup>[65]</sup>), and an output layer (180 neurons, which are batch-normalized and activated by the sigmoid function for bounded wave response values). Similarly, R2GNet is composed of an input layer (180 neurons), 6 hidden layers (120 neurons for each layer, which are all batch-normalized and activated by the GELU function), and an output layer (60 neurons, which are batch-normalized and activated by the sigmoid function, and one neuron that preserves the fixed value for the thickness  $d_{\text{GST}} = 1000$  nm).

**Calculation of the  $\tau$  Order Metric:** While the conventional translational order metric  $\tau$  is originally calculated from the pair correlation function over a continuous and infinite domain under the assumption of statistically homogeneous point processes,<sup>[40]</sup> we instead utilize the definition of the  $\tau$  metric that allows inhomogeneity of finite samples.<sup>[39]</sup> For a finite range of a 1D two-phase medium composed of alternating layers with low and high permittivities  $\varepsilon_L$  and  $\varepsilon_H$ , respectively, the indicator function for a material phase is defined as

$$I(x) = \begin{cases} 0, & \text{if } \varepsilon(x) = \varepsilon_L \\ 1, & \text{if } \varepsilon(x) = \varepsilon_H \end{cases} \quad (8)$$

where  $\varepsilon(x)$  is the permittivity landscape function with the binary value  $\varepsilon_L$  or  $\varepsilon_H$  in the finite range. By discretizing this range with  $N_s$  points, we achieve the  $\tau$  metric from the discrete Fourier transform  $\tilde{I}_k = \sum_{n=0}^{N_s-1} I_n e^{i2\pi nk/N_s}$  of the indicator array  $I_n = I(n\Delta x)$ :

$$\tau \equiv \sum_{k \neq 0} \left[ \frac{|\tilde{I}_k|^2}{N} - \left(1 - \frac{N}{N_s}\right) \right]^2 \quad (9)$$

where  $N = \sum_{n=0}^{N_s-1} I_n$  is the number of 1's in the indicator array. The order metric used in this work is an averaged value of  $\tau$  in the left and right parts of the GST layer. In Figure 5, we normalize the order metrics with  $\tau_c$ , which is the  $\tau$  value of the ideal crystal of 30 layers with a periodicity of 200 nm and  $N/N_s = 0.5$ .

**Optimization Process for Engineered Active Disorder:** To extract the optimal  $\mathbf{c}$ , we utilize the gradient ascent optimization that maximizes the correlation  $\rho_{f,X}(\mathbf{c}) = (N-1)^{-1} \sum_{i=0}^{N-1} \tilde{f}(\mathbf{s}^i; \mathbf{c}) \tilde{X}^i$  between  $f(\mathbf{s})$  and  $X = T_{\text{avg}}$  or  $\tau$  (see Note S7 in the Supporting Information), where  $i$  is the index for

$N$  data points and the tilde denotes the normalized quantity with zero mean and unit variance. While  $|\rho_{f,X}| = 1$  allows complete engineering of active disorder for each quantity  $X$ , the optimization process leads to

$$\mathbf{c}_{\text{opt}}^{(X)} = \underset{\mathbf{c}: \|\mathbf{c}\|=1}{\operatorname{argmax}} |\rho_{f,X}(\mathbf{c})| \quad (10)$$

which describes the contribution of each component in  $\mathbf{q}(\mathbf{s})$  to wave ( $T_{\text{avg}}$ ) or matter ( $\tau$ ) quantities.

## Supporting Information

Supporting Information is available from the Wiley Online Library or from the author.



## Acknowledgements

This work was supported by the National Research Foundation of Korea (NRF) through the Global Frontier Program (GFP, 2014M3A6B3063708) funded by the Korean government. S.Y. was supported by the National Research Foundation of Korea (NRF) grant funded by the Korean government (MSIT) (No. 2021R1C1C1005031 and No. 2021R1A4A3032027).

## Conflict of Interest

The authors declare no conflict of interest.

## Data Availability Statement

The data that support the findings of this study are available from the corresponding author upon reasonable request.

## Keywords

active devices, deep learning, engineered disorder

Received: December 14, 2021

Published online: February 25, 2022

- [1] F. Zangeneh-Nejad, R. Fleury, *Nat. Commun.* **2019**, *10*, 2058.
- [2] D. Ielmini, H.-S. P. Wong, *Nat. Electron.* **2018**, *1*, 333.
- [3] J. Gao, Y.-Y. Liu, R. M. D'Souza, A.-L. Barabási, *Nat. Commun.* **2014**, *5*, 5415.
- [4] X. Yang, Z. Cai, *Phys. Rev. Lett.* **2021**, *126*, 020602.
- [5] A. Tikan, J. Riemensberger, K. Komagata, S. Hönl, M. Churav, C. Skehan, H. Guo, R. N. Wang, J. Liu, P. Seidler, T. J. Kippenberg, *Nat. Phys.* **2021**, *17*, 604.
- [6] H. Cao, J. Wiersig, *Rev. Mod. Phys.* **2015**, *87*, 61.
- [7] S. Stützer, Y. Plotnik, Y. Lumer, P. Titum, N. H. Lindner, M. Segev, M. C. Rechtsman, A. Szameit, *Nature* **2018**, *560*, 461.
- [8] W. C. Chew, *Waves and Fields in Inhomogeneous Media*, Wiley-IEEE Press, Hoboken, NJ **1999**.
- [9] S. Yu, C.-W. Qiu, Y. Chong, S. Torquato, N. Park, *Nat. Rev. Mater.* **2021**, *6*, 226.
- [10] W. Man, M. Florescu, E. P. Williamson, Y. He, S. R. Hashemizad, B. Y. C. Leung, D. R. Liner, S. Torquato, P. M. Chaikin, P. J. Steinhardt, *Proc. Natl. Acad. Sci. USA* **2013**, *110*, 15886.
- [11] M. Filoche, S. Mayboroda, *Proc. Natl. Acad. Sci. USA* **2012**, *109*, 14761.
- [12] G. Lefebvre, A. Gondel, M. Dubois, M. Atlan, F. Feppon, A. Labbé, C. Gillot, A. Garelli, M. Ernoult, S. Mayboroda, M. Filoche, P. Sebbah, *Phys. Rev. Lett.* **2016**, *117*, 074301.
- [13] A. Graves, N. Jaitly, A. Mohamed, *2013 IEEE Workshop on Automatic Speech Recognition and Understanding*, IEEE, Olomouc, Czech Republic, Dec **2013**, pp. 273–278.
- [14] A. Krizhevsky, I. Sutskever, G. E. Hinton, *Commun. ACM* **2017**, *60*, 84.
- [15] X. Han, X. Wang, K. Zhou, *Bioinformatics* **2019**, *35*, 4640.
- [16] M. Lutter, C. Ritter, J. Peters, *arXiv:1907.04490*, **2019**.
- [17] S. Ha, H. Jeong, *Phys. Rev. Res.* **2021**, *3*, L042035.
- [18] P. Zhang, H. Shen, H. Zhai, *Phys. Rev. Lett.* **2018**, *120*, 066401.
- [19] J. F. Rodriguez-Nieva, M. S. Scheurer, *Nat. Phys.* **2019**, *15*, 790.
- [20] S. Yu, X. Piao, N. Park, *Nat. Commun.* **2020**, *11*, 4842.
- [21] M. Raissi, A. Yazdani, G. E. Karniadakis, *Science* **2020**, *367*, 1026.
- [22] W. Ma, Z. Liu, Z. A. Kudyshev, A. Boltasseva, W. Cai, Y. Liu, *Nat. Photonics* **2021**, *15*, 77.
- [23] J. Jiang, M. Chen, J. A. Fan, *Nat. Rev. Mater.* **2021**, *6*, 679.
- [24] Y. Xu, X. Zhang, Y. Fu, Y. Liu, *Photonics Res.* **2021**, *9*, B135.
- [25] P. R. Wiecha, O. L. Muskens, *Nano Lett.* **2020**, *20*, 329.
- [26] D. Liu, Y. Tan, E. Khoram, Z. Yu, *ACS Photonics* **2018**, *5*, 1365.
- [27] W. Ma, F. Cheng, Y. Liu, *ACS Nano* **2018**, *12*, 6326.
- [28] S. So, J. Mun, J. Rho, *ACS Appl. Mater. Interfaces* **2019**, *11*, 24264.
- [29] W. Ma, F. Cheng, Y. Xu, Q. Wen, Y. Liu, *Adv. Mater.* **2019**, *31*, 1901111.
- [30] Z. Liu, D. Zhu, K.-T. Lee, A. S. Kim, L. Raju, W. Cai, *Adv. Mater.* **2020**, *32*, 1904790.
- [31] W. Ma, Y. Liu, *Sci. China-Phys. Mech. Astron.* **2020**, *63*, 284212.
- [32] H. Ren, W. Shao, Y. Li, F. Salim, M. Gu, *Sci. Adv.* **2020**, *6*, eaaz4261.
- [33] Z. Liu, D. Zhu, S. P. Rodrigues, K.-T. Lee, W. Cai, *Nano Lett.* **2018**, *18*, 6570.
- [34] S. So, J. Rho, *Nanophotonics* **2019**, *8*, 1255.
- [35] R. Unni, K. Yao, Y. Zheng, *ACS Photonics* **2020**, *7*, 2703.
- [36] R. Unni, K. Yao, X. Han, M. Zhou, Y. Zheng, *Nanophotonics* **2021**, *10*, 4057.
- [37] J. Peurifoy, Y. Shen, L. Jing, Y. Yang, F. Cano-Renteria, B. G. DeLacy, J. D. Joannopoulos, M. Tegmark, M. Soljačić, *Sci. Adv.* **2018**, *4*, eaar4206.
- [38] C. Zhang, J. Jin, W. Na, Q.-J. Zhang, M. Yu, *IEEE Trans. Microw. Theory Tech.* **2018**, *66*, 3781.
- [39] R. A. DiStasio, G. Zhang, F. H. Stillinger, S. Torquato, *Phys. Rev. E* **2018**, *97*, 023311.
- [40] S. Torquato, *Phys. Rep.* **2018**, *745*, 1.
- [41] H. H. Sheinfux, I. Kaminer, A. Z. Genack, M. Segev, *Nat. Commun.* **2016**, *7*, 12927.
- [42] C. W. Hsu, B. Zhen, W. Qiu, O. Shapira, B. G. DeLacy, J. D. Joannopoulos, M. Soljačić, *Nat. Commun.* **2014**, *5*, 3152.
- [43] N. Aizawa, Y.-J. Pu, M. Watanabe, T. Chiba, K. Ideta, N. Toyota, M. Igarashi, Y. Suzuri, H. Sasabe, J. Kido, *Nat. Commun.* **2014**, *5*, 5756.
- [44] W. L. Chan, H.-T. Chen, A. J. Taylor, I. Brener, M. J. Cich, D. M. Mittleman, *Appl. Phys. Lett.* **2009**, *94*, 213511.
- [45] Y. LeCun, Y. Bengio, G. Hinton, *Nature* **2015**, *521*, 436.
- [46] D. Lencer, M. Salinga, B. Grabowski, T. Hickel, J. Neugebauer, M. Wuttig, *Nat. Mater.* **2008**, *7*, 972.
- [47] M. F. Yanik, S. Fan, M. Soljačić, J. D. Joannopoulos, *Opt. Lett.* **2003**, *28*, 2506.
- [48] X. Piao, S. Yu, N. Park, *Opt. Express* **2012**, *20*, 18994.
- [49] A. Komar, R. Paniagua-Dominguez, A. Miroshnichenko, Y. F. Yu, Y. S. Kivshar, A. I. Kuznetsov, D. Neshev, *ACS Photonics* **2018**, *5*, 1742.
- [50] A. M. Shaltout, V. M. Shalae, M. L. Brongersma, *Science* **2019**, *364*, eaat3100.
- [51] N. W. Ashcroft, N. D. Mermin, *Solid State Physics*, Brooks/Cole, 1st edition, Belmont, CA **1976**.
- [52] K. Chung, S. Yu, C.-J. Heo, J. W. Shim, S.-M. Yang, M. G. Han, H.-S. Lee, Y. Jin, S. Y. Lee, N. Park, J. H. Shin, *Adv. Mater.* **2012**, *24*, 2375.
- [53] A.-L. Barabási, *Network Science*, Cambridge University Press, Cambridge, UK **2016**.
- [54] W. R. Bandy, A. J. Glick, *Phys. Rev. B* **1977**, *16*, 2346.
- [55] J. B. Pendry, *J. Phys. C-Solid State Phys.* **1982**, *15*, 5773.
- [56] H. H. Sheinfux, I. Kaminer, Y. Plotnik, G. Bartal, M. Segev, *Phys. Rev. Lett.* **2014**, *113*, 243901.
- [57] S. Havlin, R. B. Selinger, M. Schwartz, H. E. Stanley, A. Bunde, *Phys. Rev. Lett.* **1988**, *61*, 1438.
- [58] F. A. B. F. de Moura, M. L. Lyra, *Phys. Rev. Lett.* **1998**, *81*, 3735.
- [59] G. K. Shirmanesh, R. Sokhoyan, R. A. Pala, H. A. Atwater, *Nano Lett.* **2018**, *18*, 2957.

- [60] S. An, C. Fowler, B. Zheng, M. Y. Shalaginov, H. Tang, H. Li, L. Zhou, J. Ding, A. M. Agarwal, C. Rivero-Baleine, K. A. Richardson, T. Gu, J. Hu, H. Zhang, *ACS Photonics* **2019**, 6, 3196.
- [61] J. Tian, H. Luo, Y. Yang, F. Ding, Y. Qu, D. Zhao, M. Qiu, S. I. Bozhevolnyi, *Nat. Commun.* **2019**, 10, 396.
- [62] S. Abdollahramezani, O. Hemmatyar, M. Taghinejad, H. Taghinejad, Y. Kiarashinejad, M. Zandehshahvar, T. Fan, S. Deshmukh, A. A. Eftekhar, W. Cai, E. Pop, M. A. El-Sayed, A. Adibi, *Nano Lett.* **2021**, 21, 1238.
- [63] Y. Sharabi, E. Lustig, M. Segev, *Phys. Rev. Lett.* **2021**, 126, 163902.
- [64] S. Ioffe, C. Szegedy, *Proceedings of the 32nd International Conference on Machine Learning (ICML 2015)*, Lille, France, **2015**, pp. 448–456.
- [65] D. Hendrycks, K. Gimpel, *arXiv:1606.08415*, **2016**.
- [66] I. H. Malitson, *J. Opt. Soc. Am.* **1965**, 55, 1205.
- [67] J. Kischkat, S. Peters, B. Gruska, M. Semtsiv, M. Chashnikova, M. Klinkmüller, O. Fedosenko, S. Machulik, A. Aleksandrova, G. Monastyrskyi, Y. Flores, W. T. Masselink, *Appl. Opt.* **2012**, 51, 6789.
- [68] T. Cao, C. Wei, R. E. Simpson, L. Zhang, M. J. Cryan, *Sci. Rep.* **2014**, 4, 4463.